*Inorg. Chem.* **2004**, *43*, 1667–1680


# Probing the Electronic Structures of Ternary Perovskite and Pyrochlore Oxides Containing $Sn^{4+}$ or $Sb^{5+}$

**Hiroshi Mizoguchi, Hank W. Eng, and Patrick M. Woodward***

*Department of Chemistry, The Ohio State University, Columbus, Ohio 43210-1185*

Received May 22, 2003

Experimental and computational studies were performed to understand the electronic structure of ternary perovskites ($ASnO_3$, A = Ca, Sr, Ba, Cd), pyrochlores ($RE_2Sn_2O_7$, RE = Y, La, Lu; $Cd_2Sb_2O_7$), and defect pyrochlore oxides ($Ag_2Sb_2O_6$) containing the main group ions $Sn^{4+}$ and $Sb^{5+}$. In all compounds, the lowest energy states in the conduction band arise primarily from the antibonding Sn/Sb 5s–O 2p interaction. In the alkaline-earth stannate perovskites ($BaSnO_3$, $SrSnO_3$, and $CaSnO_3$) the conduction bandwidth decreases strongly in response to the octahedral tilting distortion triggered by the decreasing size of the alkaline-earth cation. This in turn leads to a corresponding increase in the band gap from 3.1 eV in $BaSnO_3$ to 4.4 eV in $CaSnO_3$. The band gap of $CdSnO_3$ is relatively small (3.0 eV) considering the large octahedral tilting distortion. The origin of this apparent anomaly is the mixing between the empty Cd 5s orbitals and the antibonding Sn 5s–O 2p states. This mixing leads to a widening of the conduction band and a corresponding decrease in the band gap. The participation of the normally inert A-site cation in the electronic structure near the Fermi level can be considered an inductive effect, as it utilizes substitution on the A-site to directly modify the electronic structure of the $SnO_3^{2-}$ framework. While the pyrochlore structure is more complicated, the energy level and width of the lowest energy conduction band can be analyzed in a manner similar to that utilized on the perovskite structure. The Sn–O–Sn and Sb–O–Sb bonds are highly distorted from linear geometry in pyrochlore, leading to a relatively narrow conduction band and a wide band gap. In $Cd_2Sb_2O_7$ and $Ag_2Sb_2O_6$ the $Cd^{2+}$ and $Ag^+$ ions exhibit a strong inductive effect that widens the conduction band and lowers the band gap significantly, very similar to the effect observed in the perovskite form of $CdSnO_3$.

## 1. Introduction

There are relatively few materials that are simultaneously transparent to visible light (or a portion of the visible spectrum) and good conductors of electricity. Most of the materials that do display this behavior are n-doped metal oxides, such as $In_2O_3$, ZnO, and $SnO_2$. These materials are collectively referred to as transparent conducting oxides or TCO materials for short. Transparent conductors are utilized in a wide variety of products from photovoltaics to antistatic coatings, but the two dominant applications are in flat-panel displays and energy-efficient windows. Fluorine-doped $SnO_2$ is the most utilized material for energy-efficient window coatings, while tin-doped $In_2O_3$ (ITO) dominates the market for flat panel displays, a market that is projected to grow to over $27 billion per annum by the year 2005.[1] For applications that depend only upon the resistivity and transparency, it has proven difficult to improve upon the properties of ITO, but as TCO materials are used increasingly as an integral component in thin film devices, such as photovoltaic cells, electroluminescent flat panel displays, and light emitting diodes of various types, the need for a variety of TCO materials becomes increasingly apparent. Cost, stability in harsh environments, good lattice match, and proper energy level matching with neighboring layers in the thin film architecture all become important characteristics in the design criteria. With these considerations in mind, it is not possible for one or two materials to be optimal for all applications.

A common feature among n-type TCO materials is the presence of a metal with a $(n-1)d^{10}ns^0$ electron configuration, such as $Zn^{2+}$, $In^{3+}$, $Cd^{2+}$, $Ga^{3+}$, $Tl^{3+}$, $Pb^{4+}$, $Sn^{4+}$,[2] and most recently $Bi^{5+}$.[3] We can expand our search to include

* To whom correspondence should be addressed. E-mail: woodward@chemistry.ohio-state.edu.

(1) Ginley, D. S.; Bright, C. *Mater. Res. Soc. Bull.* **2000**, *25*, 15.

(2) Kawazoe, H.; Ueda, N.; Un'no, H.; Omata, T.; Hosono, H.; Tanoue, H. *J. Appl. Phys.* **1994**, *76*, 7935.

10.1021/ic034551c CCC: $27.50 
Published on Web 02/10/2004

other ions with similar electron configurations, such as $Sb^{5+}$. Among this list of ions, indium and gallium have become somewhat undesirable due to their high cost, while cadmium, lead, and thallium are unattractive for applications due to their toxicity. Taking these factors into account suggests that it may be fruitful to search for new TCO materials among the oxides of $Zn^{2+}$, $Sn^{4+}$, $Sb^{5+}$, and/or $Bi^{5+}$. Of these ions, the electrical and optical properties of $Sb^{5+}$ and $Bi^{5+}$ have not been thoroughly investigated.[1−7] In this paper, we compare the electronic properties of ternary $Sb^{5+}$ oxides with their $Sn^{4+}$ oxide counterparts, focusing on structures containing three-dimensional networks of corner sharing octahedra, namely the perovskite and pyrochlore structure types. Traditionally, research into TCO materials has focused on structures containing edge-sharing octahedra, but it is not obvious a priori that structures built from corner-sharing octahedra should be automatically excluded. Furthermore, the use of both "inert" ($Ca^{2+}$, $Sr^{2+}$, $Ba^{2+}$, $Y^{3+}$, $La^{3+}$, $Lu^{3+}$) and "active" ($Ag^{+}$, $Cd^{2+}$) "A-site" cations to alter the connectivity and bonding of the corner sharing octahedral network is carefully examined.

## 2. Experimental Section

Samples of $CaSnO_3$, $SrSnO_3$, $BaSnO_3$, $Y_2Sn_2O_7$, $La_2Sn_2O_7$, and $Lu_2Sn_2O_7$ were synthesized by solid state reaction at elevated temperatures. $SnO_2$ (99.9%, Fisher), $CaCO_3$ (99.9%, Mallinckrodt), $SrCO_3$ (99.9+%, Aldrich), $BaCO_3$ (99.4%, Mallinckrodt), $Y_2(CO_3)_3$ (99.9%, RE acton), $La_2O_3$ (99.99%, G. Frederick Smith Chemical), and $Lu_2O_3$ (99.9%, RE acton) were used as reagents. $La_2O_3$ was heated at 1270 K for 10 h, before weighing. These reagents were mixed in alumina pestle and mortar with ethanol. For synthesis of the stannate perovskites, the starting materials were first calcined at 1470 K for 10 h to decompose the carbonates. After the prefiring step, the obtained products were ground, pelletized, and heated at 1720 K for 15 h in air. In the case of the stannate pyrochlores, the prefiring step was not necessary, and the starting mixture was pressed into a pellet directly after grinding and treated at 1720 K for 24 h in air.

Single-phase samples of $CdSnO_3$ in its perovskite form were difficult to prepare by conventional solid state reaction. Invariably, the ilmenite polymorph of $CdSnO_3$ as well as the secondary phase $Cd_2SnO_4$ were formed in addition to the desired perovskite phase. To overcome this obstacle, we prepared $CdSnO_3$ in its perovskite form by thermal decomposition of $CdSn(OH)_6$ at 1270 K for 10 h.[8] The $CdSn(OH)_6$ precursor was synthesized hydrothermally, by reacting $K_2Sn(OH)_6$ (99.9%, Aldrich) and $Cd(NO_3)_2$ $4H_2O$ (99.9%, Mallinckrodt) in water inside a Teflon lined autoclave at 360 K for 24 h.

Solution methods starting from an $Sb_2O_5$ sol[9] were utilized for the synthesis of $Cd_2Sb_2O_7$ and $Ag_2Sb_2O_6$. $Sb_2O_3$ (0.8 g, 99.9%, Cerac) and $H_2O_2$ (20 mL) were added to water (100 mL). The suspension was stirred for 1 h at 360 K. An aqueous solution of stoichiometric $Cd(NO_3)_2{\cdot}4H_2O$ was poured slowly into the antimony oxide sol. The mixture was then heated until evaporation of the solvent was achieved. Next the obtained powder was pulverized with an alumina mortar and pestle, pressed into pellets, and heated to 1070 K for 5 h. $Ag_2Sb_2O_6$ was synthesized directly by adding $AgNO_3$ (99.9%, Alfa Aesar) to the $Sb_2O_5$ sol, without the need for further heat treatment.

Cation stoichiometries for all compounds synthesized were confirmed by X-ray energy dispersive spectroscopy with a SEM (JEOL, JSM-820 with Oxford eXL analyzer). Phase purity was checked and structure analysis carried out with laboratory X-ray powder diffraction (XRPD). XRPD data were collected in Bragg−Brentano mode with a Bruker D8 X-ray powder diffractometer (40 kV-50 mA, sealed Cu X-ray tube) equipped with an incident beam Ge 111 monochromator, which selects only Cu $K\alpha_1$ radiation, and a Braun linear position sensitive detector. Structure refinements were performed with the Rietveld method[10] as implemented in the TOPAS software package.[11]

UV−vis diffuse reflectance data were collected over the spectral range 240−1100 nm with a double beam Perkin-Elmer Lambda 20 scanning double-beam spectrometer, equipped with a 50 mm Labsphere integrating sphere, or a Perkin-Elmer Lambda 900 double beam spectrometer. MgO was used as a reference. The data were transformed into absorbance with the Kubelka−Munk function.

Band structure calculations were performed with the linear muffin-tin orbital (LMTO) method with the atomic sphere approximation (ASA) including the combined correction (CC). The LMTO-ASA code used in these calculations was developed in Stuttgart, by Andersen and co-workers.[12,13] The default number of irreducible *k*-points was used in all calculations. The basis sets consisted of the valence s, p, and d orbitals of cations and the 2s and 2p orbitals of oxygen. The Perdew−Wang exchange correlation was used.[14] Extended Huckel tight binding (EHTB) calculations were also performed in order to more accurately elucidate the bonding interactions that play a strong role near the Fermi energy. The EHTB calculations were carried out with the commercially available software program, CAESAR.[15] In the case of the pyrochlore compounds, the calculations were done on the primitive unit cell ($A_4M_4O_{14}$) in order to minimize computational time.

## 3. Results and Discussion

**3.1. Structure Description and Analysis.** The structures of $BaSnO_3$,[16] $SrSnO_3$,[17] and $CaSnO_3$[17] have been previously described in the literature. All three compounds belong to the perovskite structure class. $BaSnO_3$ has the ideal cubic perovskite structure (space group $Pm\bar{3}m$), as shown in Figure 1a. This structure is composed of a three-dimensional framework of corner-sharing $SnO_6$ octahedra, with the $Ba^{2+}$ ions filling the cubo-octahedral cavities in the structure. The


(3) Mizoguchi, H.; Bhuvanesh, N. S. P.; Woodward, P. M. *Chem. Commun.* **2003**, 1084.
(4) Yanagawa, K.; Ohki, Y.; Ueda, N.; Omata, T.; Hashimoto, T.; Kawazoe, H. *Appl. Phys. Lett.* **1993**, *63*, 3335.
(5) Yanagawa, K.; Ohki, Y.; Omata, T.; Hosono, H.; Ueda, N.; Kawazoe, H. *Jpn. J. Appl. Phys.* **1994**, *33*, L238.
(6) Yasukawa, M.; Hosono, H.; Ueda, N.; Kawazoe, H. *J. Ceram. Soc. Jpn.* **1995**, *103*, 455.
(7) Nishiyama, K.; Hattori, H. *J. Ceram. Soc. Jpn.* **2000**, *108*, 435.
(8) Levy-Clement, C.; Morgenstern-Badarau, I.; Billiet, Y.; Michel, A. *C. R. Acad. Sci.* **1970**, *270*, 1860.
(9) Brisse, F.; Stewart, D. J.; Seidl, V.; Knop, O. *Can. J. Chem.* **1972**, *50*, 3648.
(10) Young, R. A. *The Rietveld Method*; Oxford: London, 1995.
(11) Cheary, R. W.; Coelho, A. A. *J. Appl. Crystallogr.* **1992**, *25*, 109.
(12) Andersen, O. K.; Jepsen, O. *Phys. Rev. Lett.* **1984**, *53*, 2571.
(13) Andersen, O. K.; Pawlowska, Z.; Jepsen, O. *Phys. Rev. B* **1986**, *34*, 5253.
(14) Perdew, J. P.; Wang, Y. *Phys. Rev. B* **1986**, *33*, 8800.
(15) Ren, J.; Liang. W.; Whangbo, M.-H. *PrimeColor Software*; Raleigh, NC, 1998; http://www.PrimeC.com/.
(16) Smith, A. J.; Welch, J. E. *Acta Crystallogr.* **1960**, *13*, 653.
(17) (a) Vegas, A.; Vallet-Regí, M.; González-Calbet, J. M.; Alario-Franco, M. A. *Acta Crystallogr., Sect. B* **1986**, *42*, 167. (b) Green, M. A.; Prassides, K.; Day, P.; Neumann, D. A. *Int. J. Inorg. Mater.* **2000**, *2*, 35.

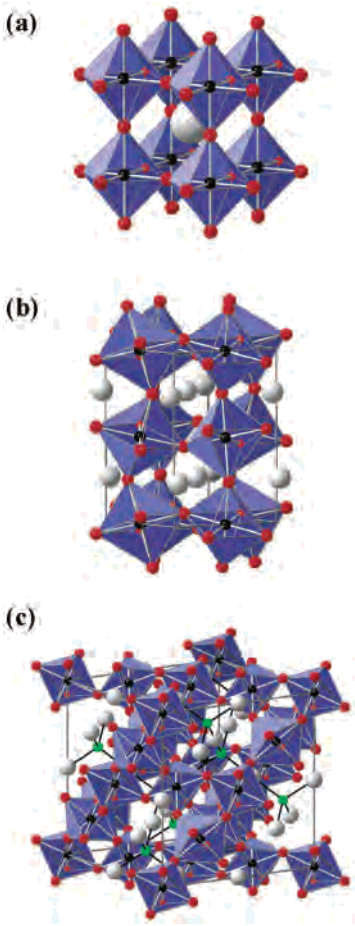


**Figure 1.** Crystal structures of (a) $BaSnO_3$, (b) $CdSnO_3$, and (c) $La_2Sn_2O_7$. The $Ba^{2+}/Cd^{2+}/La^{3+}$ ions are shown as large spheres, the $Sn^{4+}$ ions are the black spheres located at the center of the octahedra, and the oxide ions are shown as smaller red spheres at the vertices of the octahedra. The pyrochlore structure can be written as $A_2M_2O_6X'$. In part c, the X′ (=O) ions are shown as green spheres.

oxygen ions are linearly coordinated by two tin atoms. An additional four barium atoms surround each oxygen in a plane perpendicular to the Sn−O−Sn bond, but the Ba−O distances are much longer (2.905 Å) than the Sn−O distances (2.055 Å). $SrSnO_3$ and $CaSnO_3$ are both distorted from cubic symmetry by an octahedral tilting distortion. In these compounds the local octahedral environment about $Sn^{4+}$ is maintained, and the corner-sharing octahedral connectivity of the perovskite structure is also preserved, but tilts of the octahedra lead to significant changes in the environment about the A-site cation (Ba, Sr, or Ca) as well as oxygen. This type of distortion, commonly referred to as an octahedral tilting distortion, is very common in perovskites. It is driven by a mismatch in the fit of the A-site cation to the cubo-octahedral cavities in the corner-sharing octahedral network.[18] There are a number of different patterns of octahedral tilting. Glazer described 22 different types of octahedral tilting distortions,[19] and subsequently, Howard and Stokes used a group theoretical approach to show that there are only 14 unique octahedral tilting distortions.[20] In the case of $SrSnO_3$ and $CaSnO_3$, the details of the distortion are such that the crystal structure becomes orthorhombic, with *Pnma* symmetry. This type of distortion, described in Glazer notation as $a^-b^+a^-$ and shown in Figure 1b, is the most frequently observed distortion of the perovskite structure (over 50% of $AMX_3$ perovskites adopt this structure type).[21] It is typically referred to as either the $GdFeO_3$ or the $CaTiO_3$ structure type. The dimensions of the orthorhombic unit cell are $\sqrt{2}a_p \times 2a_p \times \sqrt{2}a_p$, where $a_p$ is the cell edge of the undistorted cubic structure.

**Table 1.** Crystal Structure of the Perovskite Polymorph of $CdSnO_3$[a]

| atom | Wyckoff site | $x$ | $y$ | $z$ | $U_{iso}$ (Å$^2$)[b] |
|---|---|---|---|---|---|
| Cd | 4c | 0.5423(2) | 1/4 | 0.5092(3) | 0.0084(4) |
| Sn | 4b | 0 | 0 | 1/2 | 0.0022(4) |
| O(1) | 4c | 0.955(2) | 1/4 | 0.386(2) | 0.009(1) |
| O(2) | 8d | 0.301(2) | 0.058(1) | 0.695(1) | 0.009(1) |

[a] As determined from analysis of a monochromatic Cu $K\alpha_1$ X-ray diffraction data set covering the $2\theta$ range 10−135°. (The refinements revealed 1.85(6) mol % of $Cd_2SnO_4$ as a secondary phase.) The Rietveld refinement ($R_{wp} = 16.85\%$, $R_{Bragg} = 2.37\%$, $\chi^2 = 1.30$) was carried out in space group *Pnma* with unit cell parameters of $a = 5.57524(8)$ Å, $b = 7.8711(1)$ Å, and $c = 5.45877(8)$ Å. [b] The displacement parameters for the O(1) and O(2) sites were constrained to be equal.

Unlike $ASnO_3$ (A = Ba, Sr, Ca), the detailed structure of the perovskite polymorph of $CdSnO_3$ has not previously been reported.[22,23] Thus, we applied the Rietveld technique to refine the structure of this phase from X-ray powder diffraction data. There was a small amount of $Cd_2SnO_4$ ($Sr_2PbO_4$-type struture, space group *Pbam*) impurity present, necessitating a two-phase refinement of the XRPD data. The refinements confirm that $CdSnO_3$ is a distorted perovskite, isostructural with $CaSnO_3$ and $SrSnO_3$, and that the content of $Cd_2SnO_4$ is 1.9 mol %. The results are summarized in Table 1, while the observed, calculated, and difference patterns are shown in the Supporting Information. The structure is illustrated in Figure 1b. Selected bond distances and angles are listed in Table 2 together with the previously reported structural characteristics for each of the stannate perovskites. We see that the average Sn−O distance and the octahedral environment about tin are relatively insensitive to substitutions on the A-site, but the Sn−O−Sn bond becomes increasingly distorted from linear as the size of the A-site cation decreases. Naturally, the A−O distances are also very sensitive to the size of the octahedral tilting distortion, but it is important to also recognize the change in the coordination geometry around oxygen. The size of $Cd^{2+}$ ion is somewhat smaller than $Ca^{2+}$, which drives a larger octahedral tilting distortion thereby producing shorter Cd−O bonds. This has implications for the electronic structure and optical properties that we will return to later. In an attempt to see if there was an additional "covalency" contribution to the tilting in $CdSnO_3$, we used the program SPuDS[21] to calculate expected Sn−O−Sn bond angles. The algorithms used in SPuDS are based on the bond valence

(18) Woodward, P. M. *Acta Crystallogr., Sect. B* **1997**, *53*, 44.
(19) Glazer, A. M. *Acta Crystallog., Sect. B* **1972**, *28*, 3384.
(20) Howard, C. J.; Stokes, H. T. *Acta Crystallogr., Sect. B* **1998**, *54*, 782.
(21) Lufaso, M. W.; Woodward, P. M. *Acta Crystallogr., Sect. B* **2001**, *57*, 725.
(22) Smith, A. J. *Acta Crystallogr.* **1960**, *13*, 749.
(23) Shannon, R. D.; Gillson, J. L.; Bouchard, R. J. *J. Phys. Chem. Solids* **1977**, *38*, 877.

**Table 2.** Structural Features of Ternary Stannate Perovskites, $ASnO_3$

| compd | space group | Sn−O distance (Å) | Sn−O−Sn angle (deg) | O−Sn−O angle (deg)[a] | O(4c)−A distance (Å) | O(8d)−A distance (Å) |
|---|---|---|---|---|---|---|
| $BaSnO_3$[16] (1.014)[b] | $Pm\bar{3}m$ | 6 × 2.055 | 180 | 90.0 | 4 × 2.905 | |
| $SrSnO_3$[17] (0.957)[b] | Pnma | 2 × 2.046 | 160.5 | 90.8 | 2.534 | 2.539 |
| | | 2 × 2.048 | 159.6 | 89.2 | 2.706 | 2.793 |
| | | 2 × 2.052 | | 90.2 | | 2.848 |
| | | | | 88.9 | | |
| $CaSnO_3$[17] (0.905)[b] | Pnma | 2 × 2.061 | 146.7 | 89.2 | 2.344 | 2.364 |
| | | 2 × 2.061 | 148.2 | 90.8 | 2.414 | 2.640 |
| | | 2 × 2.063 | | 87.7 | | 2.792 |
| | | | | 92.3 | | |
| $CdSnO_3$ (0.883)[b] | Pnma | 2 × 2.040(8) | 142.4 | 91.9(4) | 2.21(1) | 2.265(8) |
| | | 2 × 2.051(8) | 145.0 | 88.4(1) | 2.39(1) | 2.641(8) |
| | | 2 × 2.078(3) | | 91.6(1) | | 2.807(8) |
| | | | | 88.4(1) | | |

[a] Excluding 180° O−Sn−O angles. [b] Tolerance factor as calculated by SPuDS based on bond valence parameters.

concept;[24] consequently its estimate of the octahedral tilting distortion does not explicitly take covalency into account. The SPuDS optimized structures have Sn−O−Sn bond angles of 159.0° and 159.2° for $SrSnO_3$, 147.0° and 147.6° for $CaSnO_3$, and 142.4° and 143.3° for $CdSnO_3$. These values are in quite close agreement with the observed Sn−O−Sn angles in Table 2. Consequently, we can say that while the octahedral tilting distortion seen in $CdSnO_3$ is quite large, its value is consistent with what one would expect on the basis of the size of the $Cd^{2+}$ ion.

The second set of compounds that have been investigated in this study are members of the pyrochlore family, with $A_2M_2O_6X$ stoichiometry. Like the perovskite structure, the basic framework of the pyrochlore structure (space group = $Fd\bar{3}m$) is a three-dimensional corner-sharing network of $MO_6$ octahedra, as shown in Figure 1c. Within this framework, a three-dimensional network of channels contains the $A_2X$ sublattice. The X anion is often an oxide anion as well, but in some cases it can be fluoride or hydroxide or even vacant, as it is in $Ag_2Sb_2O_6$. The lattice oxygen atoms in the corner-sharing octahedral framework sit on the 48f Wyckoff sites, with $C_{2v}$ symmetry. They are coordinated to two M-site and two A-site cations in a highly distorted tetrahedral type environment. The structures of the $A_2Sn_2O_7$ pyrochlores have previously been determined,[25] but the detailed crystal structures of $Cd_2Sb_2O_7$[9] and $Ag_2Sb_2O_6$[26] have not been previously established. Therefore, we used XRPD and Rietveld refinements to determine the crystal structures of these two compounds. The refinement results are summarized in Table 3, while the observed, calculated, and difference patterns are shown in the Supporting Information. Selected bond distances and angles for both stannate and antimonate pyrochlores are listed in Table 4. As with perovskites, the Sn−O and Sb−O distances are relatively insensitive to changes in the A-site cation, though this distance is noticeably longer in $La_2Sn_2O_7$ than in the other two stannate pyrochlores. In sharp contrast to the perovskites, the M−O−M angles are confined to a relatively small range of values, from 125° to 135°. Thus the pyrochlore structure is more rigid and less amenable to substitutions over a wide range of ion sizes.

**Table 3.** Crystal Structures of Antimonate Pyrochlores, As Determined from Rietveld Refinements Based on Monochromatic Cu $K\alpha_1$ X-ray Diffraction Data Sets Covering the $2\theta$ Range 10−120°

| | $Cd_2Sb_2O_7$ | $Ag_2Sb_2O_6$ |
|---|---|---|
| Refinement Statistics | | |
| $R_{wp}$ | 16.80 | 10.51 |
| $R_{Bragg}$ | 1.91 | 1.94 |
| $\chi^2$ | 1.23 | 1.46 |
| Structure Variables[a] | | |
| space group | $Fd3m$ (No. 227) | $Fd3m$ (No. 227) |
| $a$ (Å) | 10.2572(2) | 10.27155(7) |
| O $x$ | 0.3236(7) | 0.3256(5) |
| Displacement Parameters | | |
| Cd/Ag $U_{iso}$ (Å$^2$) | 0.0100(8) | 0.0318(4) |
| Sb $U_{iso}$ (Å$^2$) | 0.0020(8) | 0.0042(3) |
| O $U_{iso}$ (Å$^2$) | 0.0126[b] | 0.024(3) |

[a] Wyckoff positions and occupancies the pyrochlore structure are as follows: A on the 16d site ($^1/_2$, $^1/_2$, $^1/_2$); Sb on the 16c site (0, 0, 0); O on the 48f site ($x$, $^1/_8$, $^1/_8$); and O′ on the 8b site ($^3/_8$, $^3/_8$, $^3/_8$). Note that the O′ site is vacant in $Ag_2Sb_2O_6$. [b] The displacement parameters for the O and O′ sites were fixed at this value.

**Table 4.** Structural Features of Ternary Stannate and Antimonate Pyrochlores, $A_2M_2O_6O'$

| compd | M−O distance (Å) | M−O−M angle (deg) | O−M−O angles (deg) | O−A distance (Å) | O′−A distance (Å) |
|---|---|---|---|---|---|
| $La_2Sn_2O_7$[25] | 6 × 2.074 | 131.6 | 96.47 | 2 × 2.629 | 4 × 2.317 |
| | | | 83.53 | | |
| $Lu_2Sn_2O_7$[25] | 6 × 2.040 | 126.2 | 99.96 | 2 × 2.456 | 4 × 2.228 |
| | | | 80.04 | | |
| $Y_2Sn_2O_7$[25] | 6 × 2.043 | 127.6 | 99.06 | 2 × 2.495 | 4 × 2.246 |
| | | | 80.94 | | |
| $Cd_2Sb_2O_7$ | 6 × 1.964(3) | 134.8 | 94.4(3) | 2 × 2.561(5) | 4 × 2.2208 |
| | | | 85.7(3) | | |
| $Ag_2Sb_2O_6$ | 6 × 1.975(2) | 133.7 | 95.1(2) | 2 × 2.551(4) | |
| | | | 84.9(2) | | |

**3.2. Optical Absorption.** All of the compounds studied in this work are white, with the exception of $CdSnO_3$ (dull yellow), $Cd_2Sb_2O_7$ (dull brown), and $Ag_2Sb_2O_6$ (pale yellow). To accurately quantify the optical band gaps of these compounds, diffuse reflectance spectra were collected on powder samples. The optical absorption spectra measured for perovskite or pyrochlore powders at room temperature are shown in Figure 2a,b, respectively. Numerical band gap ($E_g$) values were determined from these data and are listed in Table 5. For those compounds where band gaps had previously been reported in the literature, $BaSnO_3$, $CdSnO_3$, $Cd_2Sb_2O_7$, and $Ag_2Sb_2O_6$, our values were in reasonably good

(24) Brown, I. D. *Chem. Soc. Rev.* **1978**, *7*, 359.
(25) Kennedy, B. J.; Hunter, B. A.; Howard, C. J. *J. Solid State Chem.* **1997**, *130*, 58.
(26) Schrewelius, N. *Z. Anorg. Allg. Chem.* **1938**, *238*, 241.

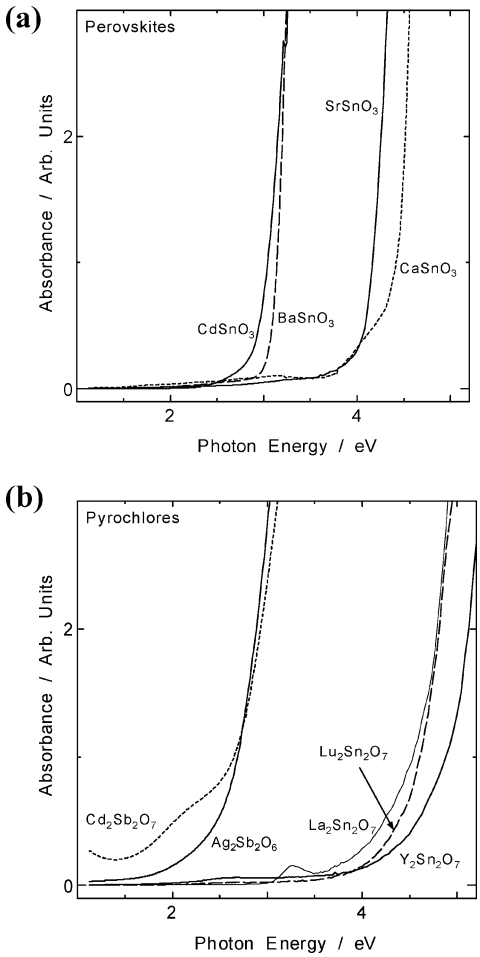


**Figure 2.** Diffuse reflectance spectra for ternary stannate and antimonate compounds belonging to (a) the perovskite family, or (b) the pyrochlore family.

**Table 5.** Optical Band Gaps, $E_g$'s, of Stannate and Antimonite Perovskites and Pyrochlores as Experimentally Determined at Room Temperature from Diffuse Reflectance Measurements on Powders[a]

| compd | exptl $E_g$ (eV) | lit. $E_g$ (eV) | calcd $E_g$ (eV) |
|---|---|---|---|
| $BaSnO_3$ | 3.1 | 3.1,[b,27] 3.4[b,28] | 0.9 |
| $SrSnO_3$ | 4.1 | | 2.5 |
| $CaSnO_3$ | 4.4 | | 2.9 |
| $CdSnO_3$ | 3.0 | 3.0[c,29] | 1.7 |
| $Y_2Sn_2O_7$ | 4.8 | | 3.6 |
| $La_2Sn_2O_7$ | 4.5 | | 3.3 |
| $Lu_2Sn_2O_7$ | 4.5 | | 3.3 |
| $Cd_2Sb_2O_7$ | 2.7 | 3.0−3.5[b,5] | 0.8 |
| $Ag_2Sb_2O_6$ | 2.7 | 3.0[d,6] | 0.1 |

[a]Values reported in earlier studies and those obtained from the LMTO calculations are given for comparison [b] Powder. [c] Single crystal. [d] Thin film.

agreement with the reported values. In the case of the $ASnO_3$ (A = Ba, Sr, Ca) perovskites the band gap increases as the magnitude of the octahedral tilting distortion increases. This effect is known in the $d^0$ transition metal oxide perovskites such as $SrTiO_3/CaTiO_3$ and $KTaO_3/NaTaO_3$.[30] It is attributed to a narrowing of the conduction band. This trend cannot be extended to $CdSnO_3$ ($E_g$ = 3.0 eV), which has the largest octahedral tilting distortion but a band gap very similar to cubic $BaSnO_3$. This effect originates from the $4d^{10}5s^0$ electron configuration of $Cd^{2+}$ and will be explored in greater detail in the next section.

Among the pyrochlores the band gaps of the rare-earth stannate family ($RE_2Sn_2O_7$) fall over a fairly narrow range. The smaller band gap of $La_2Sn_2O_7$ with respect to $Y_2Sn_2O_7$ can probably be attributed to the fact that the Sn-centered octahedra are expanded in the former compound. This decreases the antibonding Sn−O interaction and thereby lowers the energy of the conduction band. The band structure calculations support this hypothesis. However, this logic does not explain the fact that $Lu_2Sn_2O_7$ has a band gap comparable to $La_2Sn_2O_7$ rather than $Y_2Sn_2O_7$. So it would seem that factors such as the electronegativity of the rare-earth ion must be taken into consideration to explain the more subtle details of the electronic structure. If we compare the stannate pyrochlores with the stannate perovskites, we see that the pyrochlore compounds have larger band gaps than even the highly distorted $CaSnO_3$. In a simple picture, this is not a complete surprise as the Sn−O−Sn angles deviate more strongly from 180° in the pyrochlores than they do in any of the perovskites. $Cd_2Sn_2O_7$ and $Ag_2Sb_2O_6$ have band gaps that are much smaller than their isostructural stannate analogues. We feel this is due largely to the active role that $Cd^{2+}$ and $Ag^+$ play in the electronic structure near the Fermi level, similar to $CdSnO_3$. This point is investigated further in the following section.

**3.3. Band Structure Calculations.** The band gap of a semiconductor/insulator depends on the position and width of the valence band (VB) and conduction band (CB). These are the extended solid equivalents of the HOMO and LUMO in molecular compounds. To understand the relationship between chemical bonding, crystal structure, and optical band gap, we performed electronic band structure calculations. In both $AMO_3$ perovskites and $A_2M_2O_{7-x}$ pyrochlores, the A cation is typically a fairly electropositive ion. As a result, this ion makes only a minor contribution to the electronic states near the Fermi level ($E_F$), and the band gap depends primarily on the bonding within the corner-sharing octahedral network. As a first step toward understanding the electronic structure of these oxides, let us consider the electronic structure of the basic building unit of each structure, an $MO_6$ octahedron. Figure 3 shows the molecular orbital diagram of an isolated $MO_6$ octahedron, where M is a main group metal.[31] The O 2s orbitals have been omitted because their energy level is considerably lower and less important than the overlap between metal orbitals and O 2p orbitals. Nonetheless, the O 2s orbitals are not completely inert, a point we will return to later. The 5s and 5p orbitals of the main group cation (Sn or Sb) form covalent interactions with the O 2p orbitals, giving rise to bonding states and antibonding states. The M 5s orbitals have a lower energy than the corresponding M 5p orbitals, which leads to more

(27) Prokopalo, O. I.; Fesenko, E. G.; Maritskaya, M. A.; Popov, Y. M.; Smotrakov, V. G. *Ferroelectrics* **1978**, *18*, 99.
(28) Larramona, G.; Gutierrez, C.; Pereira, I.; Nunes, M. R.; da Costa, M. A. *J. Chem. Soc., Faraday Trans. 1* **1989**, *85*, 907.
(29) Myasnikov, E. N.; Spinko, R. I.; Shalaeva, E. A.; Myasnikove, T. P. *Ferroelectrics* **1998**, *214*, 177.
(30) Eng, H. W.; Barnes, P. W.; Auer, B.; Woodward, P. M. *J. Solid State Chem.* **2003**, *175*, 94.

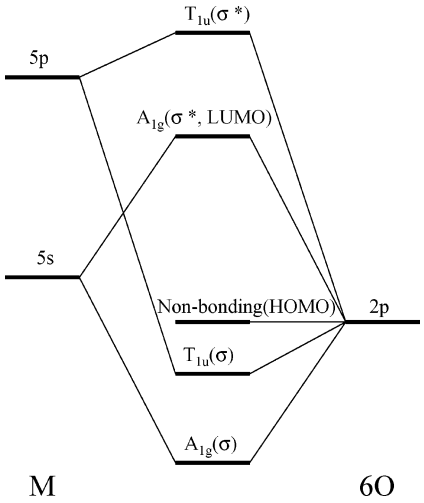


**Figure 3.** Molecular orbital diagram for an isolated $MO_6$ octahedron, where M is a main group ion. For clarity, the interaction of the O 2s orbitals has been omitted.

favorable energetic overlap of the M 5s orbitals with the more electronegative oxygen. The antibonding orbital that results from M 5s−O 2p interaction is the LUMO, while nonbonding O 2p states make up the HOMO. The M 5s orbital will make the major contribution to the LUMO, but the oxygen character makes a non-negligible contribution. This contribution will increase as the electronegativity of the metal ion increases. Nonetheless, in a loose sense the lowest energy electronic transition can be described as an oxygen to metal charge transfer transition. More accurately, it is a transition from an O 2p nonbonding orbital to an M 5s−O 2p $\sigma^*$ orbital.

While the molecular orbital picture is a useful starting point, for an extended solid band structure calculations are necessary to really understand the electronic structure. We utilized the LMTO code developed by O. K. Andersen and co-workers for band structure calculation for this purpose.[12,13] To assist in understanding the nomenclature of reciprocal space, the Brillouin zones for primitive cubic ($BaSnO_3$), primitive orthorhombic ($ASnO_3$, A = Sr, Ca, Cd), and face-centered cubic (pyrochlores) lattices are shown in Figure 4. The special points noted in these diagrams will be useful as the discussion proceeds. First of all, let us examine the agreement between the calculated and observed band gaps. Both Table 5 and Figure 5 show that the calculated band gaps are systematically related to the experimentally observed value, but the calculated band gap is consistently smaller than the observed value by approximately 1−2 eV. This level of discrepancy is not unusual for oxides. Despite the failure of the calculations to predict band gaps in an absolute sense, they do reproduce a number of the trends noted in the optical data. (1) The band gaps of the alkaline-earth stannate perovskites are seen to increase as the octahedral tilting distortion increases. (2) The presence of $Cd^{2+}$ on the A-site of the perovskite structure leads to a large decrease in the calculated band gap. (3) The presence of $Cd^{2+}$ or $Ag^{+}$ on the A-site of the pyrochlore lattice yields a much smaller calculated band gap. However, what makes the calculations most useful is the ability to pinpoint the bonding interactions

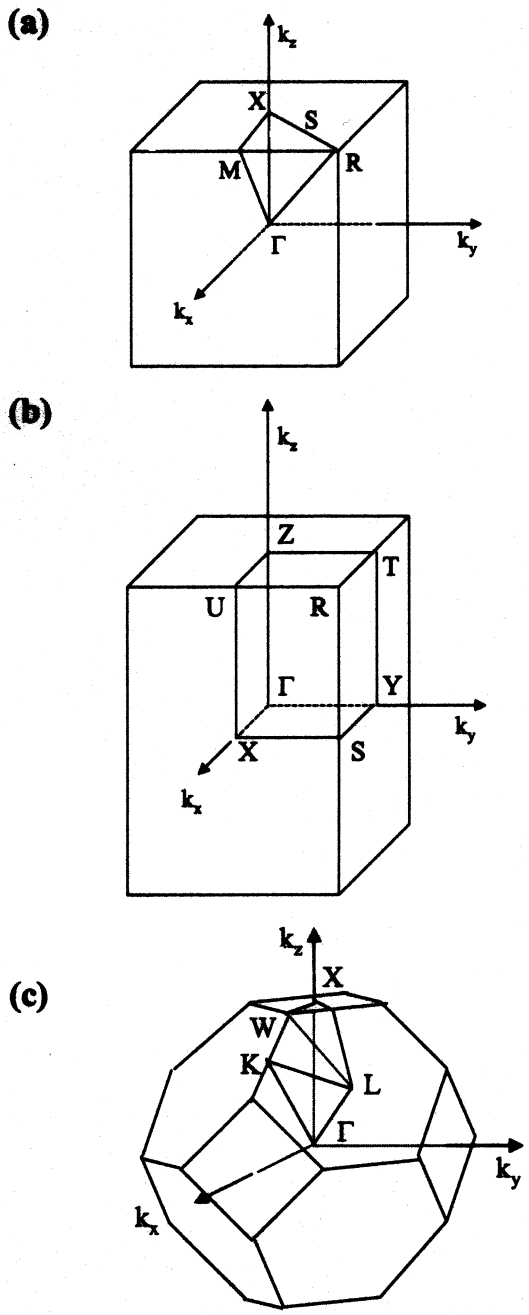


**Figure 4.** Brillouin zone of a (a) primitive cubic lattice, (b) primitive orthorhombic lattice, and (c) face-centered cubic lattice.

that control the electronic structure. To do so we need to delve deeper into the results of the LMTO calculations.

**3.3.1. Cubic Perovskite Structure: $BaSnO_3$.** The electronic band structure and density of states for $BaSnO_3$ are shown in Figure 6. In Figure 6a,b, "fatbands" are used to highlight the orbital contributions to the bands near the Fermi level. The width of the hatching corresponds to the amount of contribution of the particular atomic orbital to the band in question. Fatbands are a useful tool to quantify the change in orbital contribution from band to band, and within a given band as one moves through reciprocal space. The partial density of states (PDOS) shown in Figure 6c is simply a summation of the orbital character of all bands at a given energy. In this figure, the binding energy ($E$ = 0) is

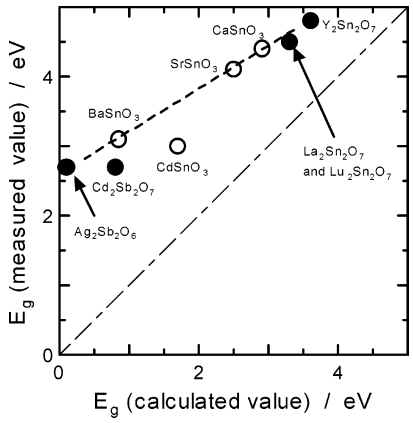


**Figure 5.** The relationship between the band gap as extracted from diffuse reflectance measurements and the band gap calculated with the LMTO code. The long−short dashed line represents perfect agreement between the two values. The upper dashed line is an empirical fit to those compounds that contain electropositive A-site cations (alkaline earth and rare-earth metal cations).

referenced to the valence band maximum. The horizontal axis scale is inversely proportional to the length of the unit cell in various directions.

For $BaSnO_3$ the valence band maximum is located at both the M and R points, while the conduction band minimum is located at the Γ point. Therefore, the calculations indicate that $BaSnO_3$ should be a semiconductor with an indirect band gap of 0.9 eV. The fatbands show that the CB minimum is predominantly Sn 5s in character with a small contribution from the O 2s orbitals. The contribution of the Ba 6s orbitals at the bottom of the CB is very small. As expected, the top of the VB is dominated by the contributions of the O 2p orbitals. This description is in qualitative agreement with the predictions of the molecular orbital diagram shown in Figure 3, with one exception. There is no O 2p contribution at the minimum of the CB. This feature originates from the translational symmetry of the cubic perovskite structure and will be discussed in greater detail below. The conduction band shows a large dispersion, particularly near the minimum at the Γ point. This suggests the carriers in doped $BaSnO_3$ should have a high mobility, because the effective mass of a carrier, $m^*$, is inversely proportional to the second derivative of the $E$ versus $k$ curve. In simple terms, very disperse bands such as this should give rise to high carrier mobility. It is well-known that high carrier mobility is a critically important property for application as a transparent conductor. It is also worthwhile to note that near the Γ point the lowest energy conduction band is separated from the next highest level by nearly 6 eV. Freeman et al. have suggested that this is an important feature of a good transparent conductor, because it limits the optical absorbance across the visible and IR regions of the spectrum.[32] So we see that the band structure of $BaSnO_3$ has features that suggest it could be a good transparent conducting oxide (TCO). In fact, n-doped $BaSnO_3$ samples (doping occurs through either $Sb^{5+}$-substitution onto the Sn-site or $La^{3+}$-substitution onto the Ba-site) are conducting.[33,34] However, to our knowledge this material has not been shown to be a particularly good TCO material. One problem may stem from the difficulty of doping a sufficient concentration of carriers into the material without simultaneously introducing recombination centers into the $SnO_3^{2-}$ framework. Aliovalent doping onto the A-site without excessive local distortion of the structure is not easy to achieve in this compound due the large size mismatch between $Ba^{2+}$ and all available trivalent ions.

Next, the origins of the CB are discussed. As stated previously, the band structure near the Fermi level originates primarily from the bonding interactions within the $SnO_3^{2-}$ framework. To deconstruct the band structure, we must consider the $\sigma$ interactions between the following sets of orbitals: Sn 5s−O 2s, Sn 5s−O 2p, and Sn 5p−O 2p. The spatial overlap of the Sn 5p−O 2p $\pi$-interaction and the energetic overlap of the Sn 5p−O 2s $\sigma$-interaction are both sufficiently weak that we can ignore these bonding interactions to a first approximation. There are equivalent Sn−O−Sn−O... chains running along the $x$, $y$, and $z$ directions in

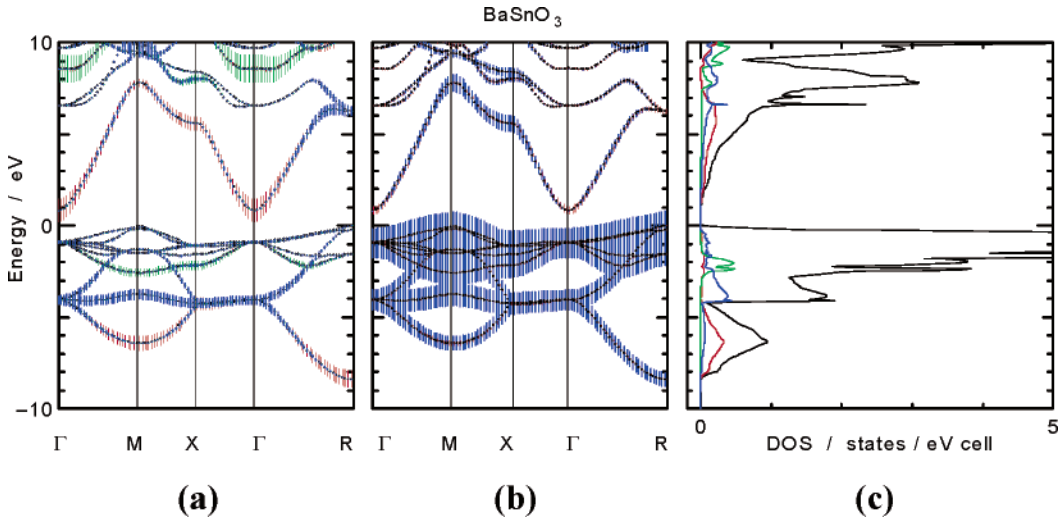


**Figure 6.** Results of band structure calculations for the cubic perovskite $BaSnO_3$. The fatband diagrams on the left-hand side show the orbital contribution of (a) the Sn 5s (red), Sn 5p (blue), and Ba 6s (green) orbitals to the band structure of $BaSnO_3$. The fatband diagrams in the middle show the O 2s (red) and O 2p (blue) contributions to the band structure of $BaSnO_3$. The density of states diagram is shown on the right-hand side. The PDOS plots show the Ba 6s contribution (green), the Sn 5s contribution (red), the Sn 5p contribution (blue), and the total electronic DOS (black).

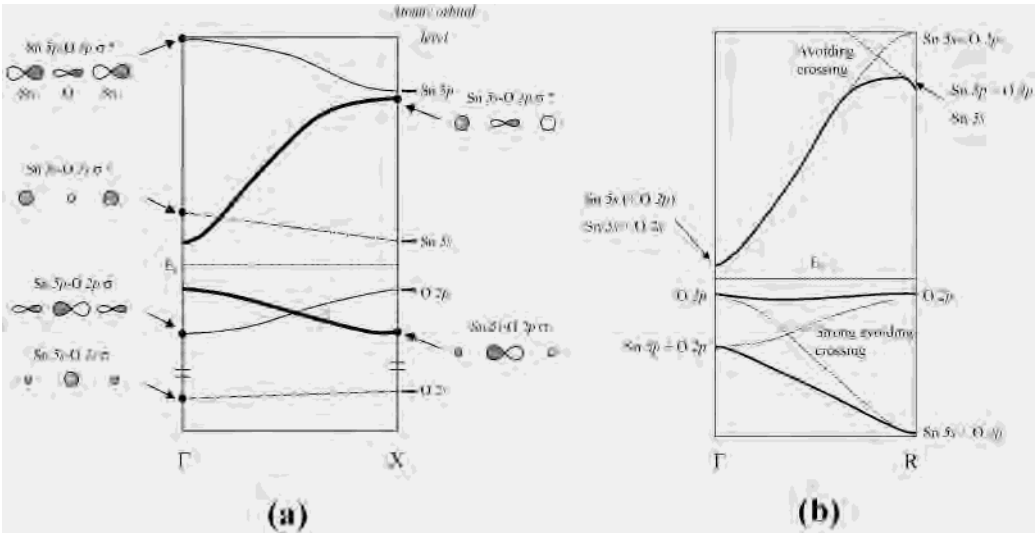


**Figure 7.** (a) Schematic one-dimensional $E$ vs $k$ diagram for Sn−O linear chain along Γ to X line. When the net overlap is zero (nonbonding), the atomic orbitals are not drawn. (b) Schematic $E$ vs $k$ diagram for $SnO_3$-unit along Γ to R line. Note that the scale is different between parts a and b.

the cubic perovskite structure (Figure 1a). Because the three directions are equivalent, we can go a long way toward understanding the band structure by considering a simple one-dimensional Sn−O chain running parallel to the *x*-axis. Figure 7a shows the orbital overlap that occurs along the Γ to X line. Because of the symmetric profile of an s orbital, the Sn 5s−O 2s interaction forms strong bonding and antibonding interactions at the Γ point, but the interaction is nonbonding at the X point. For similar reasons, the Sn 5p−O 2p $\sigma$ interaction has the same shape as the Sn 5s−O 2s interaction. On the other hand, the opposite symmetries of the s and p orbitals mean that the Sn 5s−O 2p overlap runs in the opposite sense, strong $\sigma/\sigma^*$ interactions at the X point and nonbonding at the Γ point. The band structure diagram in Figure 6 can be explained roughly through consideration of these three bonding interactions. The CB minimum at the Γ point has orbital character that is largely Sn 5s nonbonding (the O 2p contribution is zero due to symmetry) with some contribution from the O 2s orbitals through the Sn 5s−O 2s $\sigma^*$ interaction. As one moves from the Γ point toward the X point, the Sn 5s−O 2p $\sigma^*$ interaction begins to contribute and finally dominates, and the change from nonbonding to antibonding raises the energy of the band causing it to run uphill in energy. The strength of the Sn 5s−O 2p $\sigma^*$ interaction largely dictates the width of this band and is the origin of the large dispersion that characterizes the CB.

The Sn 5s−O 2p interaction is even stronger along the Γ to M and Γ to R lines because $\sigma/\sigma^*$ interactions occur not just in one crystallographic direction, but in two and three directions, respectively. This expectation is realized in the energy levels of the band that arises from the Sn 5s−O 2p bonding interaction (toward the bottom of the valence band), where this band has approximate energies of −4.1 eV at X, −6.2 eV at M, and −8.4 eV at R. However, this relation does not strictly hold if one looks at the lowest energy band in the CB, where the approximate energy levels are +5.6 eV at X, +7.8 eV at M, and +6.2 eV at R. Surprisingly, the R point has a lower energy (less antibonding) than the M point. The origin of this effect is the presence of an avoided crossing in the region of Γ to R line. As shown in Figure 7b, the Sn 5s−O 2p covalent bonding leads to a strong antibonding interaction that drives the CB to a very high energy at the X, M, and R points. At the R point, this band crosses with the Sn 5p−O 2p $\sigma^*$ band, which is antibonding at Γ but nonbonding at X, M, and R. Since both interactions have the same symmetry, crossing is forbidden, and the orbital character is exchanged at the avoided crossing point. This relation is clearly observed in the fatband depiction of Figure 6 and is the origin of the inversion of orbital energy between the M and R points. While the avoided crossing leads to a minor reduction in the overall width of the CB, it does not have a significant impact near the bottom of the CB, which is the region of the band structure that is most important in terms of the optical and electrical properties.

Next, the effect of the $Ba^{2+}$ ion on the electronic structure is briefly discussed. The atomic orbital (AO) level of Ba 5d is energetically shallow. The intense peaks located at +7 and +10 eV in the total DOS can be ascribed to Ba 5d orbitals. These peaks in the DOS arise from very flat bands in the band structure, revealing the minimal interaction between the Ba 5d and other atomic orbitals. Furthermore, the fatband diagram shown in Figure 6a reveals that Ba 6s makes only a very small contribution to the CB, consistent with expectations. The Ba 6s orbital makes a fleetingly small contribution at the CB minimum. The orbital interaction at the CBM at the Γ point is shown in diagram 1. The small contribution is due to the poor energetic and spatial overlap of the barium 6s atomic orbitals with the antibonding Sn 5s−O 2p orbitals. The Ba 6s and O 2p $\sigma$ orbitals do not mix by symmetry, and energetic overlap of the Ba 6s and O 2s

(31) Cotton, F. A. *Chemical Applications of Group Theory,* 3rd ed.; John Wiley & Sons: New York, 1990.
(32) Mryasov, O. N.; Freeman, A. J. *Phys. Rev. B* **2001**, *64*, 233111.
(33) Cava, R. J.; Gammel, P.; Batlogg, B.; Krajewski, J. J.; Peck, W. F., Jr.; Rupp, L. W., Jr.; Felder, R.; van Dover, R. B. *Phys. Rev. B* **1990**, *42*, 4815.
(34) Trari, M.; Doumerc, J.-P.; Dordor, P.; Pouchard, M.; Behr, G.; Krabbes, G. *J. Phys. Chem. Solids* **1994**, *55*, 1239.

orbitals is minimal. The poor energetic overlap can be attributed to the electropositive character of $Ba^{2+}$, while the poor spatial overlap is a characteristic feature of the cubic perovskite structure, where the A-site cation has 12 equivalent but rather long contacts with oxygen, as shown in diagram 1.

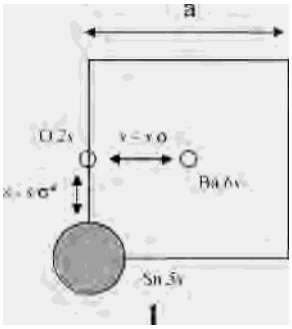


1

Finally, let us turn our attention to the chemical bonding of the O 2p orbitals. The O 2p orbitals oriented perpendicular to the M—O bond in an isolated octahedron are nonbonding (in the absence of $\pi$-bonding) and form the HOMO (see Figure 3). In an extended solid with corner-sharing octahedra, the O 2p orbitals are still nonbonding, forming a narrow band and a large localized density of states at the top of the valence band.[35,36] Although these orbitals are nonbonding with the neighboring metals, the band structure calculations show that the valence band has a small increase in energy at the M and R points. This small dispersion that occurs at the top of the VB originates from O 2p−O 2p interactions between neighboring oxide ions. The antibonding O 2p−O 2p $\sigma^*$ orbital interaction is shown in diagram 2 for the M point where the valence band maximum is located. This dispersion in the valence band is the origin of the indirect band gap calculated for $BaSnO_3$.

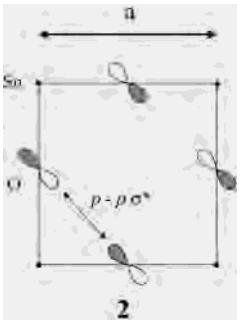


2

To first approximation, only one O 2p orbital among the three available is involved in strong $\sigma$ bonding with $Sn^{4+}$ ion. The remaining two O 2p orbitals perpendicular to Sn−O−Sn line cannot mix with Sn 5s, as pointed out by Goodenough and Kafalas.[37] This geometry is unfavorable from a covalent bonding point of view. It is offset, and the cubic perovskite structure is stabilized in $BaSnO_3$ by the favorable Madelung energy of the perovskite structure. However, as the covalency of the M—O bonding increases the cubic perovskite structure becomes increasingly unstable. To illustrate this consider the crystal chemistry of the compounds $KSbO_3$ and $NaSbO_3$.[37] Both compounds possess tolerance factors that are well suited for the perovskite structure (in fact $KTaO_3$ and $NaTaO_3$ are perovskites), but they adopt structures with edge-sharing octahedra (the cubic $KSbO_3$ structure and the ilmenite structure).

**3.3.2. The Effect of Octahedral Tilting: $CaSnO_3$.** Since over half of all perovskites, including $CaSnO_3$ and $SrSnO_3$, belong to the $GdFeO_3/CaTiO_3$ crystal structure (space group *Pnma*), it behooves us to compare and contrast the electronic structure of perovskites with *Pnma* symmetry with those possessing the aforementioned $Pm\bar{3}m$ symmetry. As shown in Table 2, when the A ion decreases in size from $Ba^{2+}$ to $Sr^{2+}$ to $Ca^{2+}$ to $Cd^{2+}$, the tolerance factor decreases, and the octahedra tilt in order to optimize the coordination environment of the smaller A-site cation. The driving forces behind this tilting have been attributed in numerous publications to the size mismatch between the A-site cation and the corner-sharing octahedral network. While ionic size considerations undoubtedly play a significant role in the crystal chemistry of $AMX_3$ perovskites, in some cases covalent interactions between the A-site cation and the anion may be important as well. We consider that effect here and its impact on the electronic structure near the Fermi level.

Although the cubic ($Pm\bar{3}m$) and orthorhombic perovskite (*Pnma*) structures are closely related, at first glance the electronic structures appear quite different. Thus, it is useful to show how the special points in reciprocal space of the cubic perovskite structure map into the orthorhombic perovskite structure. This is done in Figure 8. The untilted $Pm\bar{3}m$ perovskite structure has one formula unit per unit cell and cubic lattice parameters of $a_p \times a_p \times a_p$. The tilted *Pnma* perovskite structure has four formula units per unit cell and orthorhombic lattice parameters of $\sqrt{2}a_p \times 2a_p \times \sqrt{2}a_p$ (see Figure 1). Thus, the volume of Brillouin zone of *Pnma* (red lines in Figure 8) is one-fourth that of the $Pm\bar{3}m$ (black lines in Figure 8). Figures 6 and 9 show the *E* versus *k* plots for $Pm\bar{3}m$ and *Pnma*, respectively. The *Pnma* conduction band has four bands as a result of the fact that there are now four $Sn^{4+}$ ions in the unit cell. Upon increasing the size of the unit cell, the additional bands that appear can be explained through the concept of band folding. In Figure 8, the band folding of the CB along the Γ−X direction of the *Pnma* structure is illustrated.

Figure 9a−c shows the *E* versus *k* diagram, fatband representations, and density of states per molar unit of $CaSnO_3$ obtained from LMTO calculations. For quantitative comparison to $BaSnO_3$, the $CaSnO_3$ density of states is divided by four. As before, the valence band maximum is defined as zero for the energy axis. Although the *E* versus *k* diagram for $CaSnO_3$ looks complicated at first glance, the complexity originates from the aforementioned band folding. Once the band folding is taken into account, the electronic structure of $CaSnO_3$ is seen to be similar to $BaSnO_3$, with some notable differences. The calculations suggest that $CaSnO_3$ will be a direct-gap semiconductor with a band gap

(35) Wheeler, R. A.; Whangbo, M.-H.; Hughbanks, T.; Hoffmann, R.; Burdett, J. K.; Albright, T. A. *J. Am. Chem. Soc.* **1986**, *108*, 2222.
(36) Hughbanks, T. *J. Am. Chem. Soc.* **1985**, *107*, 6851.
(37) Goodenough, J. B.; Kafalas, J. A. *J. Solid State Chem.* **1973**, *6*, 493.

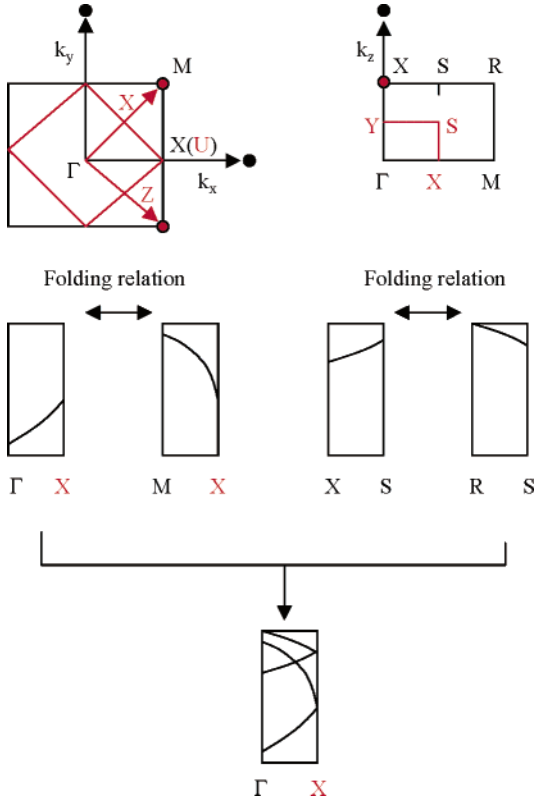


**Figure 8.** Top: conversion of Brillouin zone from $Pm\bar{3}m$ (black) to *Pnma* (red). Bottom: schematic *E* vs *k* diagram along Γ to X line in a *Pnma* perovskite for the bands near the bottom of CB.

of 2.9 eV. This value is considerably larger than the indirect band gap of $BaSnO_3$ (0.9 eV). The change from an indirect to a direct gap semiconductor originates from the band movements that accompany the band folding. The valence band maximum appears at the M and R points in $Pm\bar{3}m$, but after folding, those points move to the Γ point of *Pnma*.

The fatband representation (Figure 9a,b) shows the contributions of Sn 5s, 5p, and Ca 4s. The Sn 5s fatband splits into two regions: the Sn 5s−O 2p $\sigma$ bonding states are located in the region of −4.4 to −8.6 eV, and the antibonding states are located in the region of +2.9 to +10.1 eV. The width of the conduction band has decreased from $BaSnO_3$, where the CB spans a range from roughly +0.9 to +11.0 eV. These values show that the effect on bandwidth is most pronounced at the bottom of the CB, where it has the most significant impact on the optical and electrical properties. The valence band in the region 0.0 to −4.4 eV is composed of O 2p−O 2p weak antibonding or nonbonding states. The narrow bands that give rise to the peak seen in the density of states over the region +6 to +9 eV can be attributed to the unoccupied Ca 3d states. The lack of dispersion of these states can be attributed to the minimal orbital overlap with oxygen. A contribution from the Ca 4s orbitals can be seen at the CB minimum. This contribution is more pronounced than the one seen in $BaSnO_3$, as evidenced by the larger fatband contributions of Ca 4s orbitals (with respect to the Ba 6s orbitals). This can be attributed to the increased electronegativity of the $Ca^{2+}$ ion (better energetic overlap) and the octahedral tilting distortion (better spatial overlap). Nonetheless, the calcium contribution near the Fermi level is still relatively minor.

To understand the effect of the octahedral tilting distortion on the electronic structure more fully let us consider the orbital interactions in a linear and a zigzag Sn−O−Sn chain. Figure 10 shows a one-dimensional model of an extended cell with a doubled lattice constant (new unit cell axis, $a' = 2a_p$). The E versus *k* diagram near the bottom of the CB in the one-dimensional model is shown schematically with a solid line in Figure 10. The unoccupied 5s band of the unit cell with $a = a_p$ is folded, and the strongest Sn 5s−O $2p_x$ $\sigma^*$ band moves to the Γ′ point of the extended cell. The conduction band minimum is predominantly Sn 5s nonbonding in character, with some Sn 5s−O 2s $\sigma^*$ admixture. The band structure of the zigzag chain is shown by a dotted line. At the Γ point, the CB narrows because the distortion introduces some degree of antibonding Sn 5s−O $2p_y$ $\sigma^*$ interaction, giving rise to an increase of the band gap. In contrast, the influence of the distortion on the Sn 5s−O 2s $\sigma^*$ overlap at the CB minimum is small, because of the isotropic character of the s orbital. It is fairly straightforward to extend this effect into three dimensions, where the net result will be the same. Thus, we see that the increase of the band gap as we decrease the size of the alkaline earth cation can be explained from the standing point of tilting of the octahedral building blocks. This is an example of A-site cation substitution being used to indirectly modify the electronic structure through changes in the crystal structure. The increase in the band gap is calculated to be 2.0 eV and experimentally observed to be 1.3 eV. The discrepancy between the two values may originate from the tendency of the LMTO calculations to overestimate the bandwidth, as has been previously suggested.[30]

**3.3.3. A-Cation Inductive Effects: $CdSnO_3$.** Due to the similar crystal radii of $Ca^{2+}$ ($r$ = 1.26 Å, CN = 8) and $Cd^{2+}$ ($r$ = 1.24 Å, CN = 8),[38] the crystal structures of $CaSnO_3$ and $CdSnO_3$ are very similar. Consequently, any differences that arise in the electronic structures can be attributed to the direct influence of the *A*-site cation. Although the crystal structures of both oxides are similar, the band gap of $CdSnO_3$ (3.0 eV) is considerably smaller than that of $CaSnO_3$ (4.4 eV) (see Figure 2). This change in the band gap originates mainly from the influence of the *A* cation, as will be shown in the following discussion. Figure 9d−f shows the *E* versus *k* diagram, fatband representations, and density of states per molar unit of $CdSnO_3$ as obtained from the LMTO band structure calculation. The electronic structure of $CdSnO_3$ is qualitatively similar to the electronic structure of $CaSnO_3$. $CdSnO_3$ is a direct gap semiconductor with the conduction band minimum at the Γ point. Quantitatively, though, the calculated band gap of $CdSnO_3$ (1.7 eV) is much smaller than that of $CaSnO_3$ (2.9 eV). This cannot be explained using the Sn 5s−O 2p orbital overlap arguments of the proceeding section, because the octahedral tilting distortion is somewhat larger in $CdSnO_3$ than it is in $CaSnO_3$. However, in contrast to the expectation that the more distorted $CdSnO_3$ will have

(38) Shannon, R. D. *Acta Crystallogr., Sect. A* **1976**, *32*, 751.

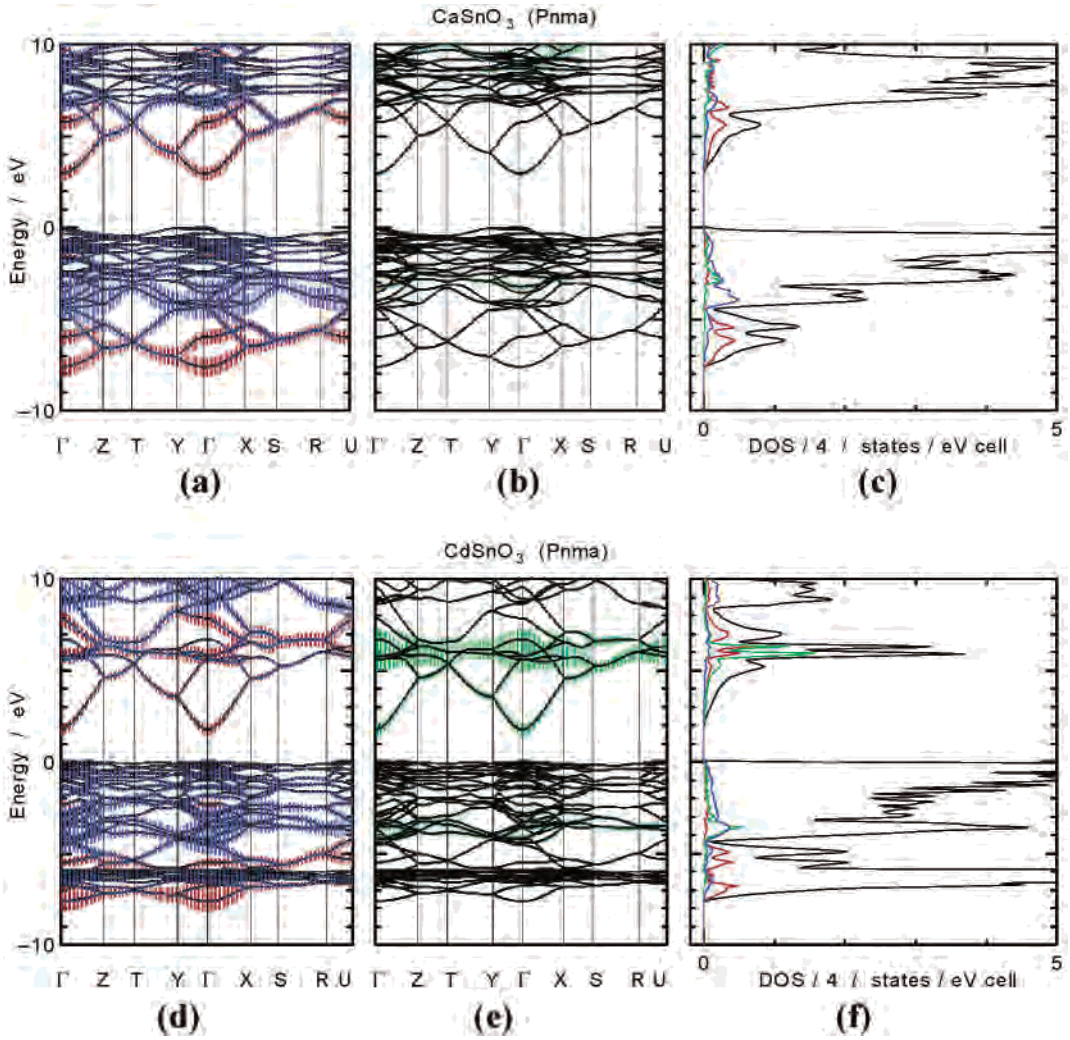


**Figure 9.** Results of band structure calculations for the distorted perovskites $CaSnO_3$ and $CdSnO_3$. The fatband diagrams on the left-hand side show the orbital contribution of the Sn 5s orbitals (red) and Sn 5p (blue) orbitals to the band structure of (a) $CaSnO_3$, (d) $CdSnO_3$. The fatband diagrams in the middle show the Ca 4s/Cd 5s (green) contribution to the band structure of (b) $CaSnO_3$, (e) $CdSnO_3$. The density of states diagrams are shown on the right-hand side for (c) $CaSnO_3$, (f) $CdSnO_3$. The PDOS plots show the Ca 4s/Cd 5s contribution (green), the Sn 5s contribution (red), the Sn 5p contribution (blue), and the total electronic DOS (black).

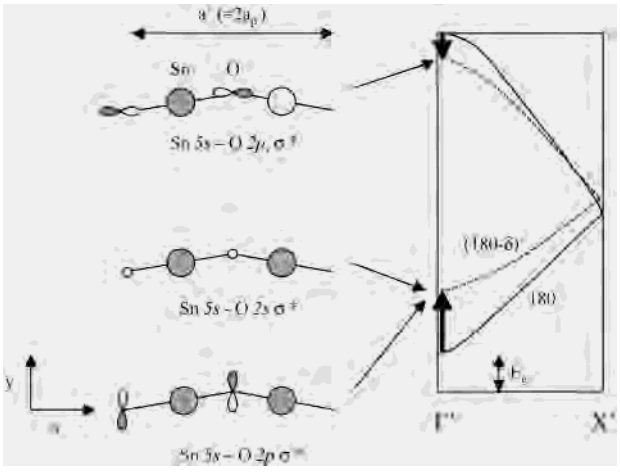


**Figure 10.** Schematic one-dimensional $E$ vs $k$ diagram along Γ′ to X′ line for Sn−O linear chain (—) and Sn−O zigzag chain (···). The bands around the bottom of CB are the only ones shown for simplicity.

a larger band gap, we see that in fact it has a much larger CB dispersion than observed in $CaSnO_3$. As was discussed for $BaSnO_3$, the large dispersion of the CB suggests that n-doped $CdSnO_3$ should possess a relatively large electron mobility. Consistent with this expectation, $CdSnO_3$ is known to be a good electronic conductor.[23] The $Cd^{2+}$ ion has fully occupied 4d orbitals located at a relatively shallow binding energy, −6.2 eV in Figure 9f. There is a possibility that the Cd 4d−O 2p interaction pushes up the valence band maximum. However, the LMTO calculation does not show any large influence from this interaction. Therefore, the band gap narrowing must be attributed to increased width of the CB. The fatbands in Figure 9d,e show that the Cd 5s and Sn 5s contribute almost equally to the lower region of the CB. Thus, we see an inductive effect (active participation of the A-site cation in bonding near $E_F$) not observed in the other $ASnO_3$ perovskites. The orbital interaction at the CB minimum (Γ point) is shown in diagram 3. As the Sn−O−Sn angle deviates from 180°, the O 2p orbital perpendicular to the Sn−Sn line can participate in the chemical bonding and the Sn 5s derived band is pushed up by this antibonding interaction. This changes the effective hybridization at oxygen from sp in the cubic structure to something closer

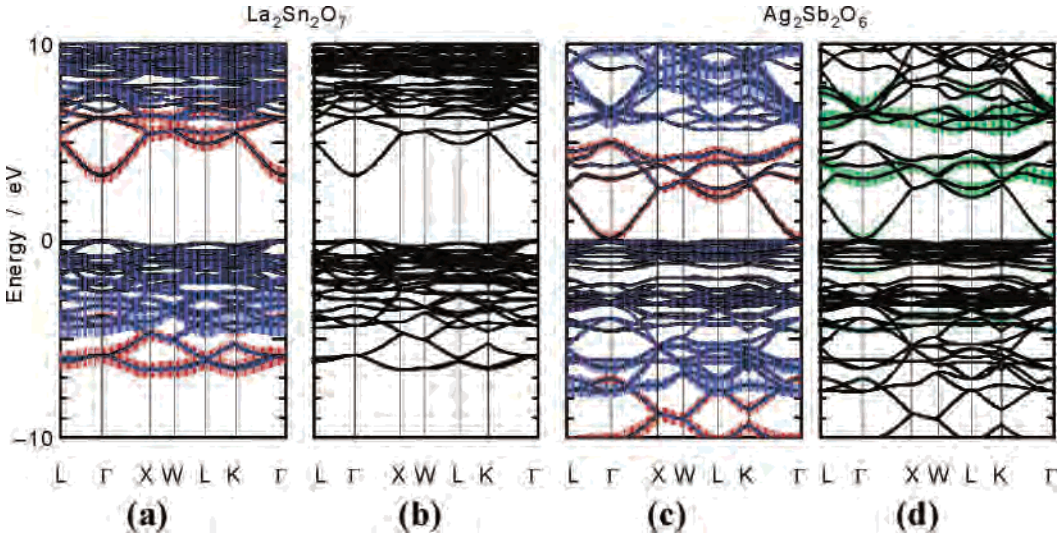


**Figure 11.** Results of band structure calculations for the pyrochlores $La_2Sn_2O_7$ and $Ag_2Sb_2O_6$. The fatband contributions are shown for (a) the Sn 5s (red) and Sn 5p (blue) orbital contributions in $La_2Sn_2O_7$, (b) the La 6s (green) orbital contribution in $La_2Sn_2O_7$, (c) the Sb 5s (red) and Sb 5p (blue) orbital contributions in $Ag_2Sb_2O_6$, and (d) the Ag 5s (green) orbital contribution in $Ag_2Sb_2O_6$.

to $sp^2$ in the heavily distorted $CdSnO_3$ structure, where the Sn−O−Sn angle is ∼140°. This value is closer to the 120° bond angle associated with $sp^2$ hybridization than the 180° angle associated with sp hybridization. [The use of the term hybridization here is meant to refer to the number of p orbitals that participate in $\sigma$ bonding with oxygen ("sp hybridization" = 2s + $2p_z$, or "$sp^2$ hybridization" = 2s + $2p_z$ + $2p_x$), and not to imply the formation of equivalent and degenerate hybrid orbitals.] At the same time, the Cd 5s orbital can form a $\sigma$-type covalent bonding interaction with the O 2p orbital that is perpendicular to the Sn−Sn line, as shown for the two crystallographically independent oxygen atoms in diagram 3. This interaction stabilizes the

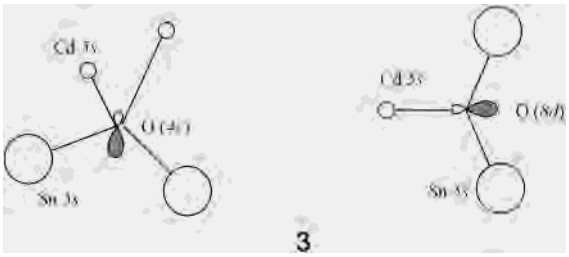


3

Sn 5s−O 2p interaction, lowering its energy. As a result, the CB dispersion increases and the band gap decreases. The inductive effect of the A-cation is evident in the partial density of states. There are several reasons for the strong inductive effect in $CdSnO_3$. First of all, the Cd 5s orbital has a good energetic overlap with the Sn 5s−O 2p $\sigma$* based CB. Second, the large octahedral tilting distortion leads to several short Cd−O contacts. Examination of the coordination environment about oxygen reveals that the short Cd−O distances (2.21 Å for O(4c) and 2.26 Å for O(8d)) are only about 10% longer than the Sn−O distances (2.04−2.08 Å). Thus in $CdSnO_3$ we get both a good spatial and energetic overlap of the Cd 5s orbitals and the antibonding Sn 5s−O 2p $\sigma$* CB states. Note that the large octahedral tilting distortion and the formation of A−O bonds go hand in hand. If a hypothetical atom existed with the size of a $Ba^{2+}$ ion and the electronegativity of the $Cd^{2+}$ ion, the inductive effect would presumably be much smaller than observed in $CdSnO_3$. In this hypothetical cubic structure, the O $2p_z$ orbital (parallel to the Sn−O−Sn bond, and the only one of the O 2p orbitals involved in bonding in the cubic structure) would not be of the correct symmetry to mix with the s orbital of the A-site cation.

**3.3.4. Stannate Pyrochlores: $La_2Sn_2O_7$.** Next, the electronic structure for the pyrochlore structure is discussed. We will start with $La_2Sn_2O_7$ because of its relatively simple and representative electronic structure. Figure 11a,b shows the *E* versus *k* diagram and fatband representations obtained from the LMTO calculations. It is a semiconductor with a large band gap (calculated value, 3.3 eV), and a conduction band minimum at the Γ point. The primitive unit cell contains four Sn atoms, and correspondingly, four bands with strong Sn 5s character are seen to make up the CB. At the Γ point, these four bands split into one weakly antibonding band at lower energy (+3.3 eV) and three more strongly antibonding degenerate bands (+6.1 eV). The bonding states also show a triple degeneracy at the Γ point, with an energy of −5.9 eV. In the previous section, the electronic structure of perovskite was explained on the basis of corner sharing $SnO_3^{2-}$ network. The electronic structure of $La_2Sn_2O_7$ can also be explained primarily from the electronic structure of the $Sn_2O_6^{4-}$ octahedral corner-sharing network. The characteristic splitting for $La_2Sn_2O_7$ at the Γ point was reproduced by the extended Hückel (EHTB) calculations of the $Sn_2O_6^{4-}$ sublattice, indicating that the contribution of $La_2O$ network into the $La_2Sn_2O_7$ electronic structure is not large near $E_F$. The La 6s fatband and partial DOS also confirm the small contribution of the La cation near the bottom of the CB. The majority of the La 6s character is distributed in bands with energies higher than +10 eV.

As shown in Figures 2 and 5, the band gaps for the stannate pyrochlores are wider than any of the stannate

perovskites. This can be understood to a reasonable approximation by considering that the connectivity of the pyrochlore lattice leads to an Sn−O−Sn bond (∼130° ) that is more distorted from linear than the values seen in the stannate perovskites, $SrSnO_3$ (156°) and $CaSnO_3$ (147°). This distortion narrows the CB width and leads to a large value of the band gap, for reasons previously put forward (see Figure 10). Unlike the perovskite structure, the connectivity of the pyrochlore lattice does not enable one to significantly alter the Sn−O−Sn angle by changing the size of the A site cation. However, Table 4 does show the possibility of stretching or compressing the $SnO_6$ octahedra by altering the size of the A site cation. Since the CB is formed from the antibonding Sn 5s−O 2p interaction, a compression of the Sn−O bond should increase the orbital overlap and the strength of the antibonding interaction, thereby raising the energy level of the CB and the size of the band gap. Such an effect is seen upon going from $La_2Sn_2O_7$ to $Y_2Sn_2O_7$.

The discussion of the preceding paragraph rationalizes the band gaps of both perovskites and pyrochlores based on the simple concept of the Sn−O−Sn angle, with no regard for the inherently different long range connectivity of the two structures. Even in a highly distorted *Pnma* perovskite it is possible to identify strings of corner sharing octahedra running independently along directions that correspond closely with the mutually orthogonal Cartesian axes. Thus, the 1D Sn−O−Sn−O−... chain analogy can reproduce the basic features of the orbital overlap fairly well. On the other hand, in the pyrochlore structure the octahedra cluster into tetrahedral units, as shown in Figure 12b. This figure shows the phases of the Sn 5s orbitals for each of the bands in the CB where these orbitals make a strong contribution. For comparison, the phases of the Sn 5s orbitals at the Γ point in an orthorhombic (*Pnma*) perovskite, such as $CaSnO_3$, are shown in Figure 12. While the corner-sharing connectivity extends in three dimensions, it is well-known that attempts to introduce long-range chemical or magnetic order onto the pyrochlore lattice are inherently frustrated due to tetrahedral connectivity of the octahedra. This raises the following question: can one relate the electronic structure of a pyrochlore to a 1D zigzag chain of corner sharing octahedra? The answer is both yes and no. At the Γ point the lowest energy configuration (in the CB) is one where all of the Sn 5s orbitals to have the same phase, as shown in Figure 12. Because all of the Sn 5s orbitals have the same phase at the Γ point, the frustration of the pyrochlore lattice is not relevant. This interaction would be nonbonding (as seen in the cubic perovskite structure at the Γ point) if all of the Sn−O−Sn bonds were linear, due to the opposite symmetries of the Sn 5s and O 2p orbitals. In reality the interaction is somewhat antibonding due to the considerable distortion of the Sn−O−Sn bonds. If we try to extend the perovskite−pyrochlore analogy to the next set of bands (at higher energy) in the CB, the similarities break down. As shown in Figure 12, there is no way to choose the phases of neighboring Sn 5s orbitals so that each of the nearest neighbor Sn 5s orbitals has the opposite phase. This gives rise to the triply degenerate set of bands that are present in both the Sn 5s−O 2p bonding and antibonding interactions at the Γ point. When we move away from the Γ point, the degeneracy is lifted, but the frustration of the pyrochlore lattice is responsible for the small dispersion of these three bands. Thus, the approach of treating the pyrochlore structure as though it were a heavily distorted perovskite only works for the lowest energy band in the CB, but fortunately, this is the most important band with regard to optical and electrical transport properties.

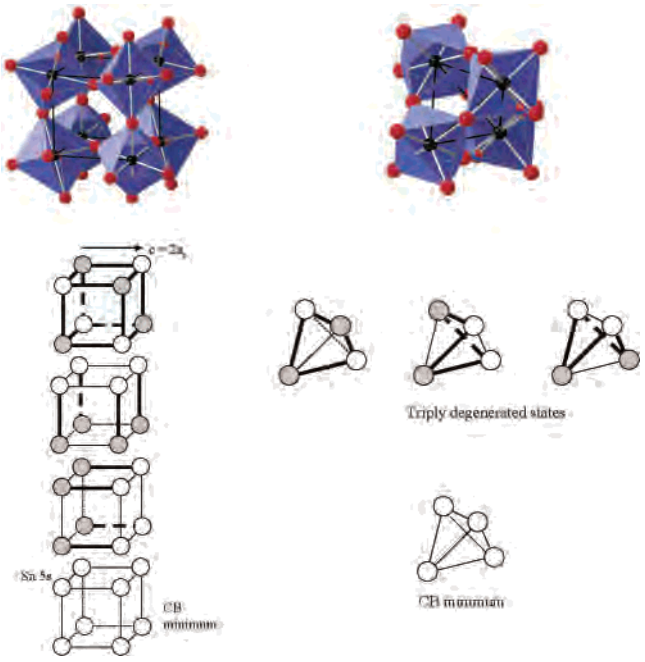


**Figure 12.** The orbital interaction for the four Sn 5s−O 2p $\sigma^*$ antibonding states in the CB of $CaSnO_3$ at the Γ point are shown on the left. Only the Sn 5s orbital character is shown for simplicity. The Sn 5s−O 2p interactions are nonbonding (linear Sn−O−Sn bonds) or weakly antibonding (bent Sn−O−Sn bonds) when the phases of neighboring Sn 5s orbitals are the same, while they are more strongly antibonding when the phases of opposite Sn 5s orbitals are opposite. The same set of orbital interactions is shown for the four Sn 5s−O 2p $\sigma^*$ antibonding states in the CB of $La_2Sn_2O_7$ at the Γ point on the left.

**3.3.5. A-Cation Inductive Effects in the Pyrochlore Structure: $Ag_2Sb_2O_6$.** Figure 11c,d shows the *E* versus *k* diagram and fatband representations for the defect pyrochlore, $Ag_2Sb_2O_6$, obtained from LMTO band calculation. The calculated band gap (0.1 eV) is much smaller than that of $La_2Sn_2O_7$ (3.3 eV), as is the experimental band gap (2.7 eV vs 4.5 eV). Perhaps not surprisingly, $Ag_2Sb_2O_6$ is known to be a TCO.[6] The smaller band gap seems to originate from

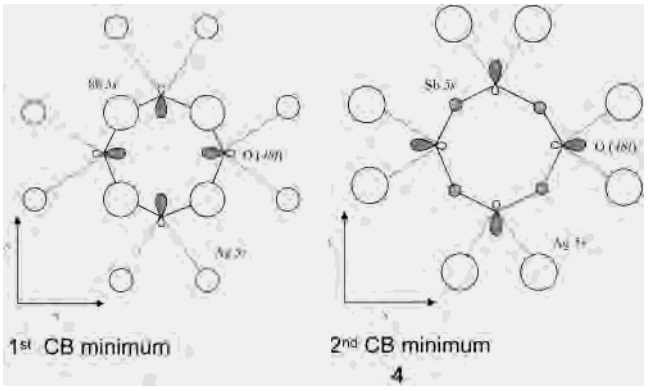

not only filled Ag 4d states located around the VB maximum, but also to a significant increase in the dispersion of the CB, particularly at the Γ point. The shape of the CB changes drastically from the basic band structure of the $Sn_2O_6$ sublattice observed in $La_2Sn_2O_7$. The origin is an inductive effect, very similar to the one previously described for $CdSnO_3$. As shown in diagram 4, there is a bonding overlap between the Ag 5s orbitals and the antibonding Sb 5s−O 2p orbitals at both the CB minimum (+0.1 eV) and the 2nd minimum (+3.1 eV). The strong mixing of Ag 5s states into the CB is clearly visible in the fatbands shown in Figure 11d.

The reasons for this inductive effect are very similar to those already elucidated for $CdSnO_3$. However, the geometry of the interaction is somewhat different in the pyrochlore structure. Here the interaction can be regarded as mixing of the electronic structures of the $Sb_2O_6$ and $Ag_2$ (or $Cd_2O$) sublattices. The interaction stabilizes the conduction band minimum, resulting in the formation of a disperse conduction band and a narrow band gap. In comparison with the distorted perovskite structure, the A−O distances are longer in pyrochlore (see Tables 2 and 4), but the site symmetries are also higher. In pyrochlore, the framework oxygen atoms sit on Wyckoff site 48f, which has $C_{2v}$ site symmetry, while in a distorted (*Pnma*) perovskite the oxygen atoms sit on Wyckoff sites 4c and 8d, which have $C_s$ and $C_1$ site symmetries, respectively. Increased dispersion and energy stabilization of the Sb 5s−O 2p bonding interaction can also be seen at the bottom of the VB (−6.2 to −11 eV for $Ag_2Sb_2O_6$ vs −4 to −6.6 eV for $La_2Sn_2O_7$). A very similar story can be used to explain the small band gap of the pyrochlore, $Cd_2Sb_2O_7$. Finally, we should comment about the band gap of $Lu_2Sn_2O_7$, 4.5 eV, which is smaller than the 4.8 eV value seen in $Y_2Sn_2O_7$ despite the similar Sn−O distances observed in both compounds. The preceding discussion suggests that it is plausible that this effect originates from a weakly covalent interaction between $Lu^{3+}$ ion and the Sn−O $\sigma^*$ states.

## 4. Conclusions

The results presented here show that the band gaps of the post transition metal perovskite ($ABO_3$) and pyrochlore oxides ($A_2B_2O_7$ and $A_2B_2O_6$) containing $Sn^{4+}$ and $Sb^{5+}$ depend on the metal−oxygen−metal bond angles as well as electronic interactions with the A-site cations mediated through neighboring oxygen atoms. For $ASnO_3$ perovskites, the band gaps increased from Ba (3.1 eV) to Sr (4.1 eV) to Ca (4.4 eV) due primarily to the decrease in Sn−O−Sn bond angle, resulting in the decrease in the conduction bandwidth. The $CdSnO_3$ perovskite had a relatively small band gap (3.0 eV) due to the inductive effect of the divalent cadmium cation, which offset the increase in band gap expected from the decrease of the Sn−O−Sn bond angle. The tin pyrochlores have still larger band gaps (∼4.5 eV). This observation can be attributed to the highly bent Sn−O−Sn bonds that are found in the pyrochlore lattice. As with the stannate perovskites, the presence of either $Cd^{2+}$ or $Ag^+$ on the A-site of the pyrochlore structure leads to a substantial decrease in the band gaps of the antimonate pyrochlores, $Cd_2Sb_2O_7$ (2.7 eV) and $Ag_2Sb_2O_6$ (2.7 eV). The LMTO band structure calculations tend to underestimate the band gaps of these materials by 1−2 eV, but they did reproduce the trends observed in the experimental band gaps. It should be noted that several of the compounds investigated here, most notably $BaSnO_3$, have disperse conduction bands. On the basis of analysis of the electronic band structure there is no apparent reason transparent conductivity cannot be found in materials with structures containing corner-sharing octahedral frameworks. However, issues related to doping and defect chemistry also need to be taken into consideration in order to gain a complete understanding of these materials.

**Acknowledgment.** First we must thank Prof. O. K. Andersen and Dr. O. Jepsen (Max Planck Institute, Stuttgart, Germany) for providing us with the LMTO codes and for support. We also thank Dr. G. D. Renkes, Dr. N. S. P. Bhuvanesh, Dr. R. L. McCreery, and Ms. A. Nowak (The Ohio State University) for experimental support. We are grateful for the help of Dr. M. Orita (HOYA Corporation) with understanding the band calculations. Finally, we are indebted to Dr. M. W. Lufaso for providing us with the SPuDS program. Financial support for this research was provided by the National Science Foundation, Grant DMR-0094271.

**Supporting Information Available:** Additional figure. This material is available free of charge via the Internet at http://pubs.acs.org.

IC034551C